Article

Ultrabroadband Terahertz Near-Field Nanospectroscopy with a HgCdTe Detector

Lukas Wehmeier,* Mengkun Liu,* Suji Park, Houk Jang, D. N. Basov, Christopher C. Homes, and G. Lawrence Carr*

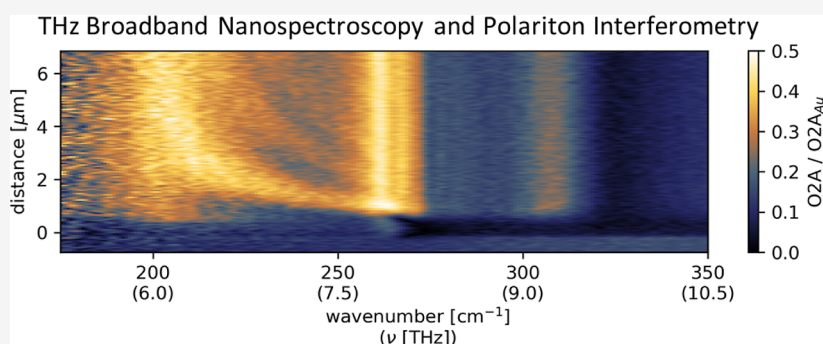Cite This: *ACS Photonics* 2023, 10, 4329−4339

Read Online

ACCESS | 📊 Metrics & More | 📖 Article Recommendations

THz Broadband Nanospectroscopy and Polariton Interferometry

ABSTRACT: While near-field infrared nanospectroscopy provides a powerful tool for nanoscale material characterization, broadband nanospectroscopy of elementary material excitations in the single-digit terahertz (THz) range remains relatively unexplored. Here, we study liquid-Helium-cooled photoconductive $Hg_{1-X}Cd_XTe$ (MCT) for use as a fast detector in near-field nanospectroscopy. Compared to the common $T = 77$ K operation, liquid-Helium cooling reduces the MCT detection threshold to ∼22 meV, improves the noise performance, and yields a response bandwidth exceeding 10 MHz. These improved detector properties have a profound impact on the near-field technique, enabling unprecedented broadband nanospectroscopy across a range of 5 to >50 THz (175 to >1750 cm^{-1}, or <6 to 57 μm), i.e., covering what is commonly known as the "THz gap". Our approach has been implemented as a user program at the National Synchrotron Light Source II, Upton, USA, where we showcase ultrabroadband synchrotron nanospectroscopy of phonons in ZnSe (∼7.8 THz) and BaF$_2$ (∼6.7 THz), as well as hyperbolic phonon polaritons in GeS (6−8 THz).

KEYWORDS: *scattering-type scanning near-field optical microscopy (s-SNOM), synchrotron infrared nanospectroscopy (SINS), terahertz, polariton interferometry, hyperbolic phonon polaritons, van der Waals materials*

INTRODUCTION

Infrared near-field nanospectroscopy combines the nanometer spatial resolution of atomic force microscopy with the high information density of optical spectroscopy. Due to its unique capabilities, the technique has continuously been expanding and has been applied to material characterization throughout various fields of engineering, chemistry, geology, and physics.[1−3] A major and rapidly growing subfield of near-field nanospectroscopy includes polariton interferometry, which provides direct access to the dispersion of deeply subwavelength-confined polariton modes.[4−13]

Many fundamental material excitations reside in the energy range of several 10 meV, e.g., phenomena related to phonons, excitons, plasmons, Landau level transitions, charge density waves, and magnons. Consequently, there is a strong desire to extend near-field nanospectroscopy toward the far-infrared and terahertz (THz) spectral range.[2,3,14] A successful approach to

this goal has been combining scattering-type scanning near-field optical microscopy (s-SNOM) with infrared radiation from accelerator-based light sources.[1−3,9,10,14−21] Specifically, synchrotron-based infrared near-field spectroscopy has pushed the spectral limit of nanospectroscopy down to ∼10 THz (320 cm^{-1}, 31 μm), thereby enabling many new experiments.[3,14−16,19−21] Additionally, coming from lower frequencies (microwave regime), nanospectroscopy and nanoimaging around and below 1 THz is nowadays more frequently achieved, e.g., via THz time-domain spectroscopy and setups based on
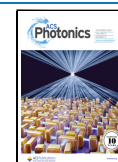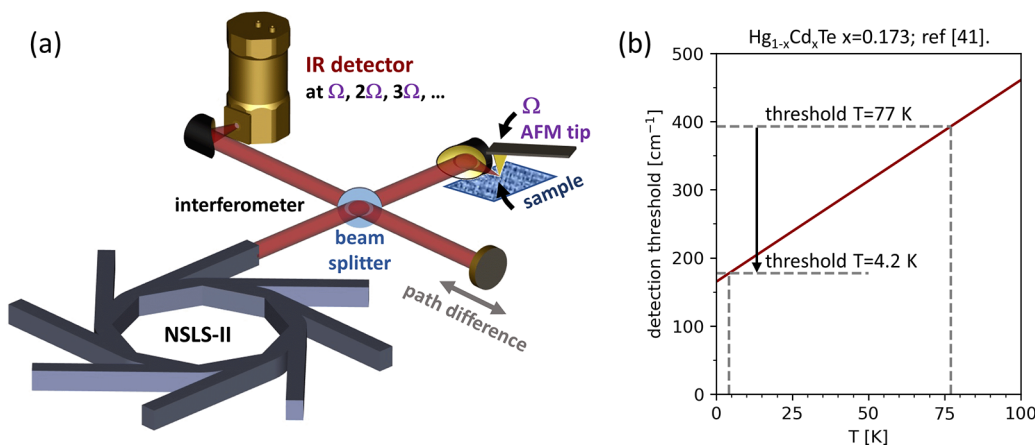
Figure 1. (a) Sketch of the near-field nanospectroscopy setup at the National Synchrotron Light Source II (NSLS-II). Infrared synchrotron radiation is guided via an asymmetric Michelson interferometer and focused onto an atomic force microscopy (AFM) tip. The latter is vibrating at frequency Ω (tapping mode). Light scattered from the tip is guided to a suitable detector as described in the main text. Near-field contributions to the detected signal are separated from the far-field background via lock-in demodulation of the detector signal at harmonics $n\Omega$ of the tip frequency with $n = 1,2,3,\cdots$ The experimental near-field data shown in this paper uses $n = 2$. (b) Calculated band gap for a $Hg_{1-x}Cd_xTe$ (MCT) infrared detector element for $x = 0.173$ as a function of temperature below 100 K; based on ref [41]. Cooling MCT to $T = 4.2$ K shifts its detection threshold to <200 cm^{-1} (>50 μm, <6 THz).

Schottky diodes or photoconductive antennas.[22−29] Despite such advances, the lack of suitable sources and matching detectors in the 1−10 THz range—the so-called "THz gap"[2,3,30] —has so far hampered extending broadband near-field nano-spectroscopy into the center of this important spectral region. While examples of near-field nanospectroscopy and polariton interferometry in the 1−10 THz spectral range do exist,[9,10,18,31−38] such studies usually employ high-intensity narrowband laser sources to compensate for less-than-ideal detectors, thereby inducing limitations for spectroscopy.

The most common method for achieving near-field infrared nanospectroscopy at mid- to far-infrared wavelengths involves the scattering of infrared light from the tip of an atomic force microscope (known as "apertureless scattering"), while the tip tracks the surface of a material in tapping mode.[2,15,39,40] Figure 1a illustrates the implementation of this scheme at the National Synchrotron Light Source II (NSLS-II), Upton, USA. The light scattered from the oscillating tip is not a simple sinusoid due to the interaction of the tip with a material, and a more localized response is recovered by demodulating the signal at the second or third harmonic of the tapping frequency.[39] With typical AFM tapping frequencies in the range of up to 300 kHz,[2,15] the detector for sensing the scattered infrared radiation requires a response bandwidth approaching 1 MHz.

The commonly employed spectral range covers wavelengths from 3 to 16 μm (625 to 3300 cm^{-1}, 19 THz to 100 THz), for which fast photodiodes made from both III−V and II−VI compound semiconductors are commercially available. Detectors for reaching into the far-infrared include the II−VI alloy mercury−cadmium-telluride ($Hg_{1-x}Cd_xTe$ or MCT) operating at $T = 77$ K for wavelengths λ out to $\lambda \sim 24$ μm (417 cm^{-1}, 12 THz; x near 0.174) and doped (i.e., extrinsic) germanium or silicon operated at $T = 4.2$ K for reaching $\lambda \sim 30$ μm (330 cm^{-1}, 10 THz). These types of detectors have been used successfully for near-field nanospectroscopy in combination with the broadband, high radiance infrared produced as synchrotron radiation.[1,3,14,42] Another extrinsic photoconductor, Ge/Ga, operates over a somewhat limited spectral range below $\lambda \sim 120$ μm. Though successfully used with narrowband free-electron laser sources down to $\lambda \sim 30$ μm,[9,10,18,34−36] there has not been

reported measurement results for the synchrotron source. Extending infrared broadband nanospectroscopy to longer wavelengths has been a challenge as the standard detector for reaching to 50 μm and beyond, the doped silicon composite bolometer operating at $T = 4.2$ K, has a response time measured in hundreds of microseconds, so it is orders of magnitude too slow for detection at AFM tip modulation frequencies. Faster thermal detectors, such as InSb hot electron bolometers (HEB), can achieve the necessary speed but the HEB effect is limited to very long wavelengths. Superconducting transition edge bolometers can also be fast but tend to have a limited dynamic range as well as challenges in manufacture.

One aspect of the $Hg_{1-x}Cd_xTe$ system that is less well-known is the dependence of the band gap and detection threshold as a function of temperature.[41,43,44] In many semiconductors, lowering the temperature causes the band edge to shift to higher energies. However, for $Hg_{1-x}Cd_xTe$ with $x < 0.5$, the band edge shifts to lower energies with decreasing T.[41,43−45] This was previously noted by the Soleil synchrotron infrared group for a mid-infrared detector intended for high spectral resolution applications.[45] Typical values for x in commercial detectors range from 0.2 to 0.17 for a detection threshold in the far-infrared. When operated at $T = 77$ K, the threshold for $x = 0.173$ is near 400 cm^{-1}. However, as illustrated in Figure 1b, by cooling this material to about 4.2 K, its threshold shifts down to below 200 cm^{-1}.[41]

In this work, we test the operation of a photoconductive MCT element having x near 0.173 at its nominal operating temperature of $T = 77$ K and when cooled with liquid helium (lHe) to about $T = 4.2$ K. Details of the experimental realization of our detector setup are described in Methods. In agreement with the known band gap dependence on temperature (Figure 1b),[41] the detection threshold for $T = 4.2$ K shifts down to below 200 cm^{-1}. Additionally, similar to the observations of the Soleil group,[45] the detector signal-to-noise shows improvement. Overall, we find that the performance of the detector is well-suited for infrared near-field nanospectroscopy down to around 175 cm^{-1} (5.2 THz, 57 μm), i.e., well into the single-digit THz range. We demonstrate this via point nanospectroscopy measurements on Au, ZnSe, and BaF$_2$ as well as polariton
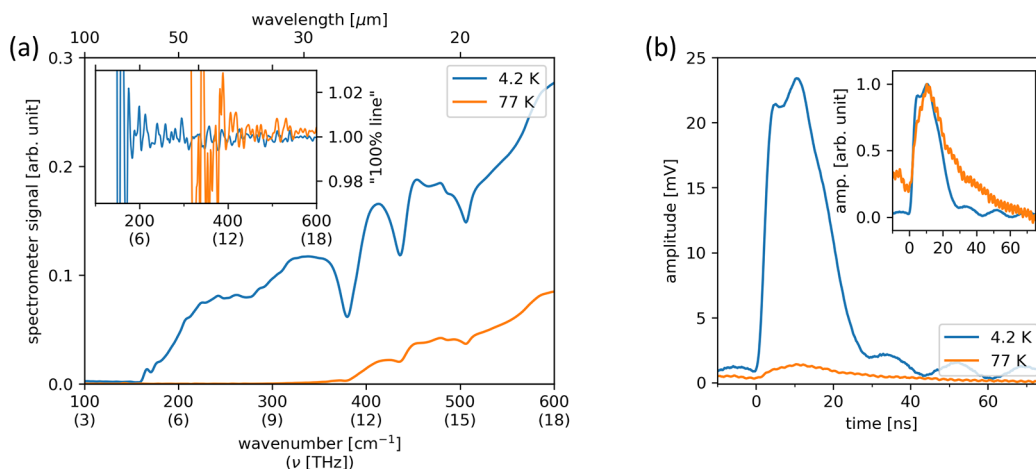
Figure 2. Far-field characterization of the detector performance. (a) Non-normalized far-field FTIR spectra acquired with our modified MCT detector cooled to either $T = 4.2$ K (1 mm aperture, blue line) or $T = 77$ K (2 mm aperture, orange line). When cooled with lHe (4.2 K), the detection threshold redshifts to around 160 cm^{-1}, and the overall detector sensitivity is significantly increased. The local minima in the 350 to 550 cm^{-1} range are due to the spectrometer's multilayer mylar beamsplitter. Inset: measured "100% line" as described in the main text. For negligible spectral drift, deviations from unity provide an estimate of the overall system noise. (b) Measurement of a short isolated 10 ps light pulse using the MCT detector cooled to $T = 4.2$ K (blue) and $T = 77$ K (orange), respectively. At lHe temperature, both sensitivity and speed are significantly increased. For the inset, both curves are scaled and offset for a better comparison of the response speed.

interferometry of the hyperbolic phonon polaritons in GeS in the 6−8 THz range.

RESULTS

Far-Field Characterization of Detector Performance. Our far-field characterization of the detector performance consisted of measuring the spectral response, the signal-to-noise, and the response speed at both $T = 77$ K and $T = 4.2$ K.

Spectral Response and Signal-to-Noise. The spectral range for the photoconductive response was measured by using a Bruker Vertex 80v spectrometer. Due to the limited availability of the synchrotron light source, we used the spectrometer's internal infrared source for this measurement. While a better signal-to-noise ratio could be obtained by employing the high spectral radiance of the synchrotron light source, here, this is not required for evaluating the detector's spectral response. Figure 2a shows the resulting spectra for operation of our modified MCT detector at $T = 77$ K and $T = 4.2$ K. The lower operating temperature reduces the detection threshold to around 160 cm^{-1} and significantly increases the overall response. The inset in Figure 2a shows a "100% line" that has been obtained by taking the ratio of two spectra acquired sequentially with identical measurement parameters. As an ideal system should yield the same result for two such measurements, deviations from unity can be attributed to either spectral drift or the noise of the overall system. The 100% lines in Figure 2a illustrate both the redshift of the detection threshold as well as the better signal-to-noise ratio for operation at lower temperature. Note that the aperture for the measurement at $T = 77$ K was 2 mm, while it was only 1 mm for $T = 4.2$ K. As the data has not been scaled to compensate for this, this means the $T = 4.2$ K is for about 4× less intensity than the $T = 77$ K data but still shows better signal-to-noise ratio, even in the higher-frequency range, e.g., around 600 cm^{-1}. When integrated over the entire spectral range (to several thousand cm^{-1}, refer to Methods), the signal-to-noise ratio can be quantified to be ~5× better for operation at $T = 4.2$ K despite the lower photon flux of the measurement.

Response Speed. Since the response bandwidth is important for the apertureless scattering method, we measured

the detector rise and fall times using a single isolated light pulse from the NSLS-II synchrotron storage ring. The pulse itself has an RMS length of about 10 ps, i.e., sufficient for measuring response up to tens of GHz. We used a Femto DHPCA-100 preamplifier set to a frequency response of 80 MHz along with a 1 GHz bandwidth oscilloscope and observed an exponential decay of (20 ± 10) ns at $T = 77$ K, corresponding to an (8 ± 4) MHz bandwidth (Figure 2b). At $T = 4.2$ K, the fall time was (7 ± 3) ns, corresponding to (21 ± 8) MHz bandwidth. Thus, the response bandwidth increased by a factor of 2−3 going from 77 to 4.2 K. We do not offer a theoretical analysis of the intrinsic relaxation (recombination) time for MCT as a function of T and x, but note that listed response times for commercial detectors show a trend of faster performance as the band gap becomes smaller. That the photoconductive response magnitude increased for lower T suggests an improved carrier mobility, offsetting the reduced photocarrier density that would stem from a faster relaxation (i.e., carrier recombination) time.

Mid-Infrared-to-THz Near-Field Nanospectroscopy. Its low-energy detection threshold, high sensitivity, good signal-to-noise ratio, and high detection speed make lHe-cooled MCT a very suitable detector for ultrabroadband nanospectroscopy down to the single-digit THz range. As a direct demonstration of our system's capabilities, we show different ultrabroadband nanospectroscopy results, namely, point spectroscopy of a gold reference sample, spectra of the THz phonon-induced near-field resonances in ZnSe and BaF$_2$ and polariton interferometry of THz phonon polaritons in GeS. Near-field nanospectroscopy is performed using a commercial near-field microscope (NeaSnom by Attocube) at the infrared MET beamline of the NSLS-II synchrotron, Upton, USA (sketch of the experimental setup in Figure 1a); to allow for ultrabroadband operation, we use a diamond beamsplitter. The near-field data shown in the paper are demodulated at the second harmonic of the tip tapping frequency.

Nanospectroscopy of Gold Reference. As gold provides a spectrally flat infrared response, measuring the spectrum of a gold reference sample allows us to determine the overall spectral response. The latter combines spectral contributions from the

broadband synchrotron radiation, absorption features of the optical elements and the system atmosphere, the s-SNOM tip, and the detector response. Figure 3a shows a gold reference point spectrum as measured with our nanospectroscopy system at NSLS-II: We obtain a near-field signal well above the noise level down to about 175 cm^{-1} (5.2 THz, 57 μm). Note that this exceeds the previous spectral limit of synchrotron infrared nanospectroscopy of 320 cm^{-1} (9.7 THz, 31 μm)[14] by almost an octave. Also, this demonstrates the extension of nanospectroscopy well into the so-called THz gap from 1 to 10 THz,[30] a spectral region that historically has been very challenging to access with near-field techniques.[2,3]

THz Phonon-Induced Near-Field Resonances. ZnSe and BaF$_2$ have widespread application as optical materials in the mid-infrared spectral range, e.g., as windows or beam splitters. While transparent in the mid infrared, both materials provide a clear phonon resonance at <300 cm^{-1}.[46,47,51] Here, we probe the phonon polariton modes of ZnSe and BaF$_2$ as an example for two materials whose polaritonic responses were previously not accessible via broadband infrared nanospectroscopy.

Figure 3b,c shows the measured near-field amplitude point spectra of ZnSe and BaF$_2$ in the broad spectral range from 175 to 1200 cm^{-1} (5.2 to 36.0 THz). While both materials are spectrally flat at higher frequencies, at <300 cm^{-1} (<9.0 THz), they show a peak of the near-field amplitude. For ZnSe and BaF$_2$, the maximum of this peak is observed at 222 cm^{-1} (6.7 THz, 45.0 μm) and 259 cm^{-1} (7.8 THz, 38.6 μm), respectively. As previously observed for other materials,[2,14,17,18,40,48,49,52] this can be attributed to phonon polariton modes inducing a resonant tip−sample near-field interaction. Note that the precise spectral peak position and width as well as the relative peak height are known to depend on experimental parameters such as the tip shape, tip tapping amplitude, average tip−sample distance, and the harmonic order used for lock-in demodulation.[3,17,49,52,53] Nevertheless, the spectral positions of the near-field resonances provide an excellent way for nanoscale material characterization[3,14,40] and, here, match well to the expectation from literature phonon parameters of ZnSe and BaF$_2$.[46,47,51] As a rule-of-thumb, the near-field resonance is expected in the spectral range where the real part of the permittivity ε' (insets of Figure 3b,c) is in the range $-10 < \varepsilon' < -1$.[18,48−50] This explains why the phonon-induced near-field resonance for BaF$_2$ is observed at higher frequency than the resonance for ZnSe, although the BaF$_2$ transverse optic (TO) phonon mode itself is observed at a lower frequency.[46,47,51]

Each spectrum in Figure 3 has a spectral resolution of 3.3 cm^{-1} and has been obtained in a measurement time of 10 min, thereby demonstrating ultrabroadband mid-infrared-to-THz nanospectroscopy at reasonable signal-to-noise ratio and spectral resolution without the need for extreme integration times. Depending on the requirements for a specific experiment, the signal-to-noise ratio can be further increased at the cost of longer integration times.

THz Hyperspectral Polariton Interferometry. GeS is a semiconducting van der Waals material (band gap around 1.6 eV[54,55]) with many intriguing properties such as an exceptional Seebeck coefficient,[56] monolayer ferroelectricity,[57] and moiré physics in twisted nanowires.[58] Its stacking direction is along the crystalline [001] direction, and exfoliated flakes show highly in-plane anisotropic polariton dispersion,[10] which is potentially field-tunable.[10,54,55] The combination of these properties makes GeS a promising platform for versatile polariton control.[10] Along GeS's [010] crystalline direction, polariton modes have been
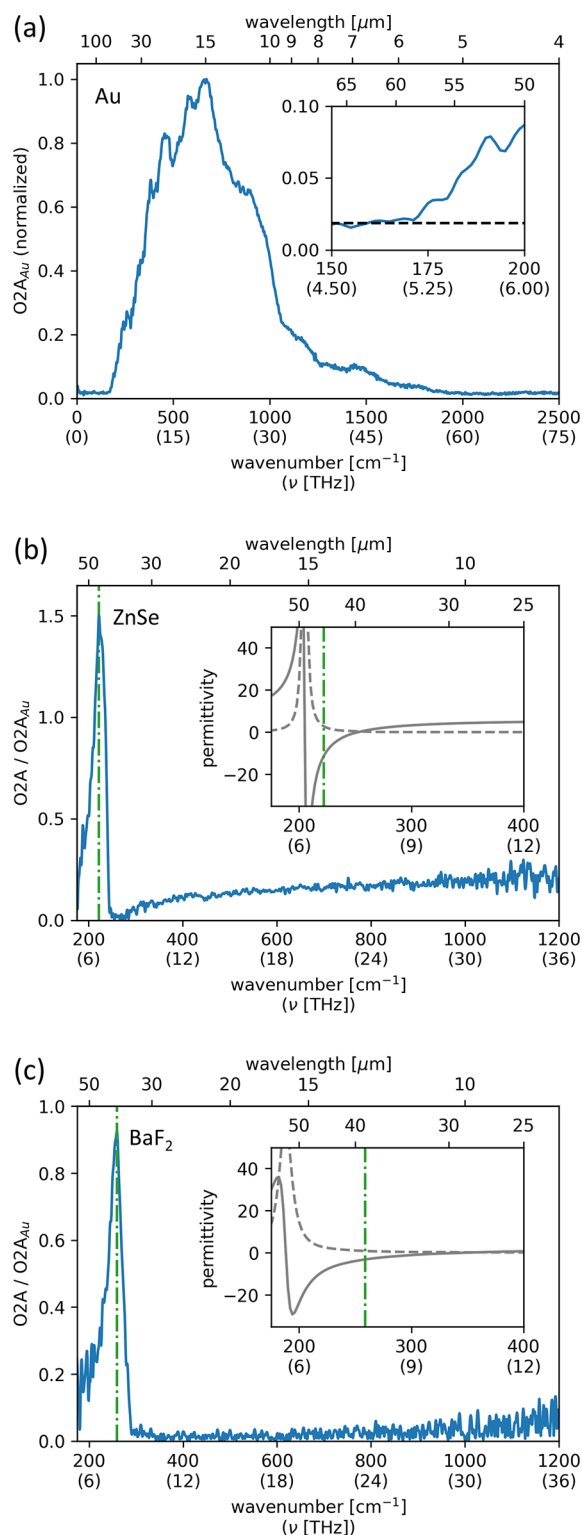

Figure 3. Midinfrared-to-THz near-field nanospectroscopy with the AFM tip at a fixed sample position (point spectroscopy). (a) Near-field amplitude spectrum of a gold reference sample illustrating the broad spectral response of our system. The system covers the spectral range from about 175 to beyond 1750 cm^{-1}, i.e., a full order of magnitude. Inset: detailed view of the low-frequency onset. The dashed horizontal line marks the noise floor. (b,c) Measured near-field amplitude of (b) ZnSe and (c) BaF$_2$ in the spectral range from 175 to 1200 cm^{-1} (5.2−36.0 THz). Each spectrum has been obtained within 10 min measurement time at a resolution of 3.3 cm^{-1}. The near-field amplitude is normalized to a spectrum taken on a separate gold reference sample.

Figure 3. continued

For both materials, phonon-induced resonant tip−sample interaction results in a peak of the normalized amplitude in the spectral range from 200 to 300 cm^{-1} (6−9 THz, approximate peak position marked by a green dash-dotted line). For comparison, the insets show literature values[46,47] for the real part (full line) and imaginary part (dashed line) of the dielectric permittivity in the spectral range of the phonon modes. While the specific position of the phonon-polariton-induced near-field resonance depends on experimental parameters and the complex dielectric material permittivity, as a rule-of-thumb, the resonance is expected in the spectral range where the real part of the permittivity ε' is in the range $-10 < \varepsilon' < -1$.[18,48−50]

observed down to 6.1 THz, thereby extending to lower frequencies than in the other in-plane direction.[10] Hence, the hyperbolic polariton modes along the [010] direction of GeS provide a model system to demonstrate polariton interferometry in the <10 THz spectral range.

Figure 4a,b shows the topography and homodyne near-field image of an exfoliated GeS flake (thickness of 149 nm) on SiO$_2$/Si substrate (sample preparation described in Methods). The homodyne near-field signal is acquired while keeping fixed the position of the interferometer reference mirror. A hyperspectral linescan with 3.3 cm^{-1} spectral resolution (Figure 4c,d) and 50 nm pixel size was measured along the crystalline [010] direction as marked by the blue arrow in Figure 4b. Figure 4c provides an overview of the near-field amplitude (top) and phase (bottom) in the broad spectral range from 175 to 1200 cm^{-1}; the spectral (spatial) information is displayed along the horizontal (vertical) axis. Positive distances refer to a position on the GeS crystal; negative values refer to a position on the SiO$_2$ substrate. SiO$_2$ shows three well-studied phonon-induced near-field resonances at around 500, 800 cm^{-1} (weak amplitude, refer to phase signal), and 1100 cm^{-1}.[14,40] While GeS itself shows no phonon modes at >400 cm^{-1},[59−61] the influence of the SiO$_2$ substrate also modulates the near-field response acquired on the GeS crystal. At lower frequencies, GeS phonon modes induce a strongly anisotropic hyperbolic infrared response.[10,59−61] As shown in the zoom-in of the near-field signal in the low-frequency spectral region from 175 to 350 cm^{-1} in Figure 4d, here, the phonon modes are apparent from a clear modulation of the GeS near-field response. Notably, in the spectral range from about 200 to 260 cm^{-1} (6.0−7.8 THz, 38−50 μm), a clear fringe pattern is observable both in the near-field amplitude and phase measured on the GeS crystal. This fringe pattern can be attributed to interference patterns caused by hyperbolic phonon polaritons propagating along the [010] direction of GeS.[10] The dispersion of these polaritons modes, i.e., their decreasing wavelength with increasing photon energy, can be directly seen in the measurement. For a detailed description of these polariton modes, we refer to ref 10. Compared to previous studies with a high-intensity narrowband laser source,[10] we emphasize that the present study demonstrates the first broadband nanospectroscopy of the GeS polariton modes as well as the first interferometric study, resolving both near-field amplitude and phase of the modes.

■ DISCUSSION AND CONCLUSIONS

We have tested liquid-helium-cooled photoconductive MCT (Hg$_{1-X}$Cd$_X$Te with x near 0.173) for usage as a fast detector for far-infrared near-field nanospectroscopy in the single-digit THz frequency range. Building up on previous literature re-

sults,[41,43−45] we found that cooling MCT down to 4.2 K lowers its detection threshold to 22 meV. In addition, compared to operation at 77 K, we found that cooling MCT to 4.2 K increased both its sensitivity and speed. This suggests a strongly improved carrier mobility that overcompensates for the reduced photocarrier density expected from faster carrier recombination. The combination of increased detector sensitivity and speed will be beneficial for various mid- to far-infrared optical techniques that require a fast response time. This potentially includes any optical setup that currently employs a lN$_2$-cooled MCT detector, i.e., both far- and near-field imaging and spectroscopy techniques. Note that the increased detector responsivity also covers the mid-infrared spectral range around 1000 cm^{-1} (30 THz, 10 μm, refer to Methods and ref 45), which is a common spectral range for many table-top near-field imaging and nanospectroscopy setups.[2] Going beyond the conventional spectral range covered by MCT detectors, we demonstrate that the properties of our specific lHe-cooled MCT detector are well suited for near-field nanospectroscopy down to 175 cm^{-1} (5.2 THz, 57 μm). Further extension of this spectral range to even lower THz frequencies may be achieved via the optimization of the MCT stoichiometry. Here, near-field point nanospectroscopy down to the single-digit THz range is demonstrated for different samples (Au reference, BaF$_2$, ZnSe). For ZnSe and BaF$_2$, we observe a phonon-induced resonant near-field interaction around 222 cm^{-1} (6.7 THz, 45.0 μm) and 259 cm^{-1} (7.8 THz, 38.6 μm), respectively. The good signal-to-noise ratio of our measurements also enables us to take hyperspectral linescans with high spectral (3.3 cm^{-1}) and spatial resolution (50 nm pixel size for a 7.5 μm long linescan). We use this for polariton interferometry of the hyperbolic phonon polariton modes of GeS in the 6 to 8 THz frequency range, resolving both the near-field amplitude and phase of these modes.

While here we demonstrate synchrotron-based THz nanospectroscopy, we emphasize that our detector system is expected to work equally well for laser-based THz nanoimaging and nanospectroscopy setups, e.g., based on free-electron-lasers,[9,10,18,34−36] gas lasers,[31,33,62] or THz quantum cascade lasers.[32,37,38] The high signal-to-noise ratio of our measurements implies that our technique will also provide great opportunities for studying the THz polariton dispersion in other van der Waals and two-dimensional materials, e.g., in graphene,[28,36] black phosphorus,[6] transition metal dichalcogenides,[29] or topological insulators such as Bi$_2$Se$_3$.[6,32,33] Furthermore, access to a plethora of new phenomena is expected when combining the here presented ultrabroadband THz nanospectroscopy with extreme sample environments in cryogenic[29,63−68] or magnetic[69,70] near-field microscopy. For example, this may enable the nanoscopic exploration of Cooper-pair and Josephson plasmon polaritons in superconductors that exclusively reside in the THz range.[6,7,71] Overall, our work demonstrates the extension of broadband infrared near-field nanospectroscopy well into the single-digit THz range, thereby significantly extending the possibilities for nanoscale optical material characterization and probing fundamental collective excitations at their natural length and energy scales.

The near-field nanospectroscopy setup built for the present work is available for general user operation at the 22-IR infrared beamline of the National Synchrotron Light Source II. Proposals can be submitted free of charge via an online proposal system.
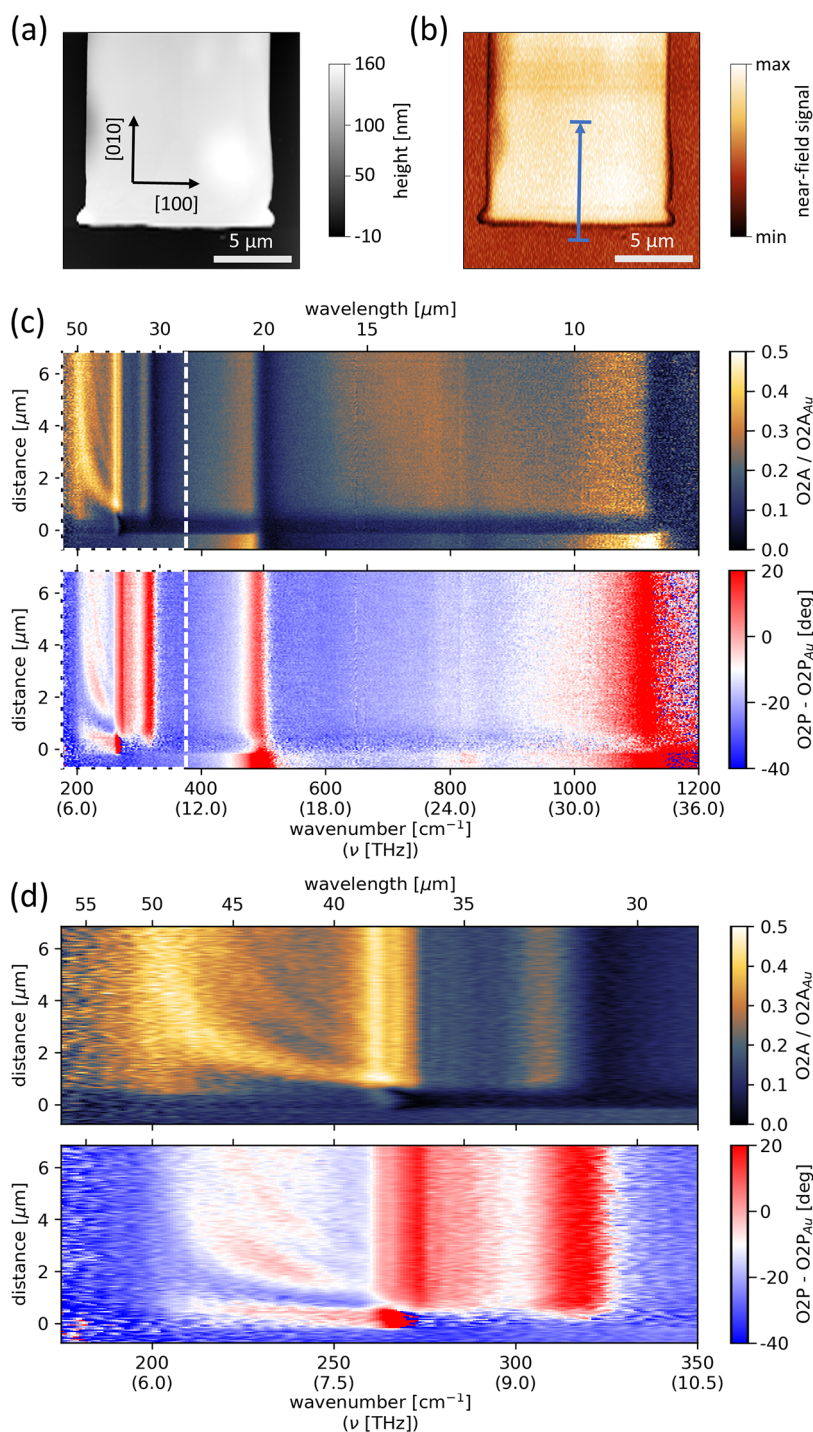
Figure 4. (a) Topography of a 149 nm thick GeS flake on a SiO$_2$ substrate. Black arrows mark the crystallographic [100] and [010] directions of GeS. (b) Homodyne (whitelight) near-field image taken simultaneously to (a). The blue arrow marks the position and direction of the hyperspectral linescan shown in (c,d). (c) Near-field amplitude (top) and phase (bottom) of a hyperspectral linescan taken along the crystallographic [010] direction of GeS as marked by the blue arrow in (b). The spatial dimension of the linescan is shown in the vertical direction; positive distances refer to a position on the GeS crystal; negative values refer to a position on the SiO$_2$ substrate. The spectral dimension of the linescan is shown in the horizontal direction; the spectral resolution is 3.3 cm^{-1}. SiO$_2$ shows three well-studied phonon resonances at around 500, 800 cm^{-1} (weak amplitude, refer to phase signal), and 1100 cm^{-1}.[14,40] GeS shows polariton modes only at lower frequencies.[10,59−61] (d) Zoom-in of the low-frequency region (175−350 cm^{-1}) of the near-field amplitude and phase spectra as marked by a white-dashed box in (c). A clear fringe pattern can be observed in the spectral range from about 200−260 cm^{-1} (6.0−7.8 THz), which can be attributed to hyperbolic phonon polariton modes propagating along the [010] direction of GeS.[10]

■ METHODS

Detector System Details. The photoconductive MCT detector for this study was a commercial model purchased from Infrared Associates. Listed as a "D24", it is intended for reaching

to approximately $\lambda \sim 24$ μm or frequencies near 400 cm^{-1} (12.5 THz), corresponding to an alloy composition x near 0.173.[41] The detector assembly, including its ceramic chip carrier mount and field-of-view (FOV) limiting aperture (see Figure 5a), was
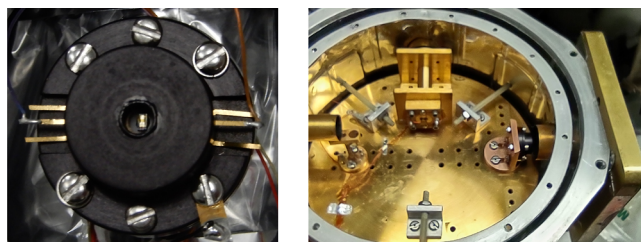
Figure 5. (a) MCT detector package from Infrared Associates including a FOV limiting baffle and electrical connections (only two are needed). The MCT photoconductive element itself is the small, bright object inside and behind the baffle's circular aperture. The ceramic chip carrier is hidden behind the FOV baffle. (b) MCT detector package mounted to an oxygen-free high-thermal-conductivity copper bracket (just right of center) bolted onto the cold plate of the *l*He reservoir. The CsI window is mounted in the gold-anodized flange at the right edge. A separate Si/B photoconductive detector assembly is near the top and includes a Winston cone optic (cylindrical object) and integrating cavity (inside the small square block with four bolts).

removed from its *l* N_2 dewar and mounted onto an oxygen-free high-thermal-conductivity copper bracket attached to the copper cold plate of an Infrared Laboratories HDL-5 liquid helium cryostat, as shown in Figure 5b. A Winston cone collector was not used, as the detector package was not compatible with the nominal integrating cavity used at the cone's exit. However, the field-of-view (FOV) limiting aperture provided by the original manufacturer was retained.

A 2 mm thick CsI disk was used for the infrared vacuum window on HDL-5, providing good transmission to about 160 cm^{-1} (63 μm, 4.8 THz), as shown in Figure 6. For testing at T = 77 K rather than at T = 4.2 K, the *l* He reservoir was filled with *l* N_2.
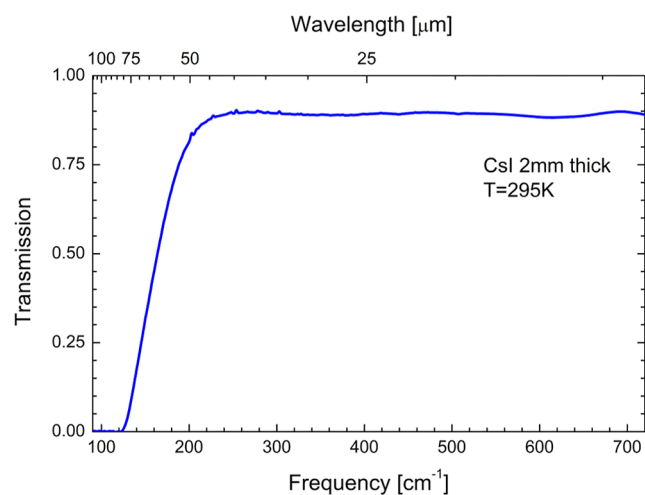

Figure 6. Measured far-infrared transmission for the cesium iodide vacuum window used on the HDL-5 detector cryostat. CsI transmits well (~90%) up through visible light frequencies.

The spectral range for the photoconductive response was measured by using a Bruker Vertex 80v spectrometer. Due to limited availability of the synchrotron light source, we used the spectrometer's internal infrared source for this measurement. While a better signal-to-noise ratio could be obtained by employing the high spectral radiance of the synchrotron light source, here, this is not required for evaluating the detector's spectral response. Figure 7 shows the same measurement as
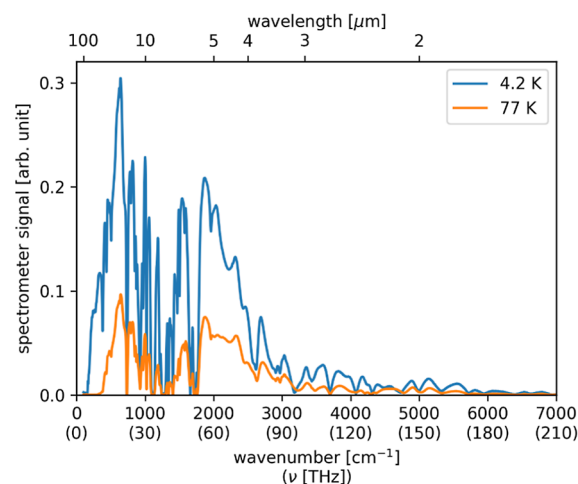

Figure 7. Non-normalized far-field FTIR spectra acquired with our modified MCT detector cooled to either T = 4.2 K (1 mm aperture, blue line) or T = 77 K (2 mm aperture, orange line). When cooled with *l*He (4.2 K), the detection threshold redshifts to around 160 cm^{-1}, and the overall detector sensitivity is significantly increased. The local minima at various frequencies throughout the spectrum are due to the spectrometer's multilayer mylar beamsplitter. Figure 2 shows a detailed view of the low-frequency region <600 cm^{-1}.

Figure 2a, i.e., a comparison between the MCT detector response when operated at either T = 77 K or T = 4.2 K. While Figure 2a shows the low-frequency region at <600 cm^{-1} to better illustrate the redshift of detection threshold, Figure 7 shows the detector response in the full spectral range up to 7000 cm^{-1}. We chose a multilayer mylar beamsplitter for this measurement, which is a good choice for the low-frequency spectral range shown in Figure 2a. However, we note that this beamsplitter is not optimized for the mid-infrared spectral region where it induces various local minima in the measured response, most pronounced in a broad frequency region around ~1000 cm^{-1}. Note that we employed a diamond beamsplitter for the near-field measurements, i.e., the minima apparent in Figure 7 do not impact the near-field response shown in Figures 3 and 4. Despite the beamsplitter being optimized for the far-infrared spectral range, Figure 7 clearly demonstrates the detector responsivity enhancement in an ultrabroad spectral range: we find that cooling the detector to T = 4.2 K enhances the detector response in the full accessible spectral range up to several thousand wavenumbers, as previously noted for a MCT detector with slightly different stoichiometric composition.[45] This suggests applications of *l*He-cooled MCT detectors also in the mid-infrared spectral range, with signal-to-noise improvement both for far-field[45] and near-field techniques. To further test the responsivity enhancement of the detector, we performed separate measurements under even more controlled conditions (broadband response measurement using a thermal source with fixed aperture, optical chopper, and lock-in detection). One goal of these separate measurements was to minimize potential impacts on the measured detector responsivity that may be expected due to the different photon fluxes incident on the detector (Auger recombination). As such, the photon flux incident on the detector was kept constant for the separate measurements. Some minor impact on the "effective" photon flux (as seen by the detector) may still originate from the shift of the low-frequency cutoff. However, the photon flux in the spectral range between ~160 cm^{-1} (cutoff at 4.2 K) and ~400 cm^{-1} (cutoff at 77 K) is much smaller than the photon flux in the

large detected spectral region >400 cm^{-1} such that a measurement at constant incident photon flux remains meaningful. While we believe that a detailed study of the photon-flux-dependent detector response is beyond the scope of the current paper (to be published elsewhere), we note that our broadband study at constant incident photon flux gave a factor of 10 higher signal for operation at 4.2 K compared to 77 K, which is not inconsistent with the results shown in Figures 2a and 7.

We compared our modified *l*He-cooled MCT detector with the response of a more common *l*He-cooled Si/B photoconductor. Note that the latter has an f/4 Winston cone to limit the FOV to ±7°, reducing the background infrared reaching the detector. The MCT detector, with its simpler ±15 °FOV limiting aperture, had at least 4 times more background falling on the detector element. As such, the comparison is more qualitative than quantitative. For both detectors, Figure 8 shows
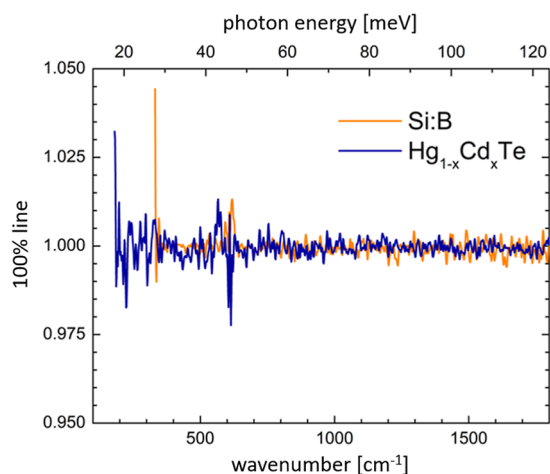

Figure 8. Measured "100% line" of our modified *l*He-cooled MCT detector in comparison to a more common *l*He-cooled Si/B photoconductor.

a measured 100% line as described in the main paper. For the specific detector setups used here, we find that the Si/B provides a better signal-to-noise ratio in the spectral range from just above its cutoff frequency at around 320 cm^{-1} to about 800 cm^{-1}; both for frequencies below and above this range, the MCT provides a better signal-to-noise ratio despite the larger background infrared falling onto the MCT detector.

Sample Preparation: GeS Exfoliation. GeS flakes were mechanically exfoliated using an automatic mechanical exfoliation machine, or an exfoliator,[72] one of the home-built modules in the Quantum material press (QPress) facility in the Center for functional nanomaterials (CFN) at Brookhaven National Laboratory (BNL). The exfoliator utilizes a roller assembly to control conditions such as the pressure, temperature, rolling and peeling speed, and peeling force. The exfoliation process has two main steps. First, the GeS bulk crystals (2D Semiconductors) were distributed on blue dicing tape and loaded onto the sample stage of the exfoliator. The exfoliator transferred the crystals on the built-in blue tape. Then, we replace the tape with bulk crystals on the sample stage on a diced 285 nm SiO$_2$-coated Si wafer chip (10 mm × 10 mm) attached to a sample holder. The exfoliator conducted the exfoliation automatically. In each step, we used the conditions for the GeS crystal transfer and exfoliation provided by the facility. After the exfoliation, the SiO$_2$ chip with exfoliated flakes was scanned by the optical

microscope of the cataloger module (WiTec Alpha 300RA) in the QPress.

■ AUTHOR INFORMATION

Corresponding Authors

Lukas Wehmeier − *National Synchrotron Light Source II, Brookhaven National Laboratory, Upton, New York 11973, United States; Department of Physics and Astronomy, Stony Brook University, Stony Brook, New York 11794, United States;* ● orcid.org/0000-0001-8416-953X; Email: lwehmeier@bnl.gov

Mengkun Liu − *National Synchrotron Light Source II, Brookhaven National Laboratory, Upton, New York 11973, United States; Department of Physics and Astronomy, Stony Brook University, Stony Brook, New York 11794, United States;* Email: mengkun.liu@stonybrook.edu

G. Lawrence Carr − *National Synchrotron Light Source II, Brookhaven National Laboratory, Upton, New York 11973, United States;* Email: carr@bnl.gov

Authors

Suji Park − *Center for Functional Nanomaterials, Brookhaven National Laboratory, Upton, New York 11973, United States;* ● orcid.org/0000-0002-2269-7705

Houk Jang − *Center for Functional Nanomaterials, Brookhaven National Laboratory, Upton, New York 11973, United States*

D. N. Basov − *Department of Physics, Columbia University, New York, New York 10027, United States*

Christopher C. Homes − *National Synchrotron Light Source II, Brookhaven National Laboratory, Upton, New York 11973, United States*

Complete contact information is available at:
https://pubs.acs.org/10.1021/acsphotonics.3c01148

Author Contributions

L. Wehmeier, M.K. Liu, D.N. Basov, and G.L. Carr conceived the project and designed the experiments. L. Wehmeier, S. Park, and H. Jang prepared the GeS sample. L. Wehmeier and G.L. Carr performed the experimental measurements and analyzed the experimental data with support from M.K. Liu and C.C. Homes. L. Wehmeier and G.L. Carr cowrote the manuscript with input from all coauthors.

Notes

The authors declare the following competing financial interest(s): S. Park has a patent pending regarding the exfoliator used for the GeS exfoliation (patent application number PCT/US2022/040777, filing date 08/18/2022; international publication number WO2023/2023260A2, publication date 02/23/2023). All other authors declare no competing interests.

■ REFERENCES

(1) Bechtel, H. A.; Muller, E. A.; Olmon, R. L.; Martin, M. C.; Raschke, M. B. Ultrabroadband Infrared Nanospectroscopic Imaging. *Proc. Natl. Acad. Sci. U.S.A.* **2014**, *111* (20), 7191−7196.

(2) Chen, X.; Hu, D.; Mescall, R.; You, G.; Basov, D. N.; Dai, Q.; Liu, M. Modern Scattering-Type Scanning Near-Field Optical Microscopy for Advanced Material Research. *Adv. Mater.* **2019**, *31*, 1804774.

(3) Bechtel, H. A.; Johnson, S. C.; Khatib, O.; Muller, E. A.; Raschke, M. B. Synchrotron Infrared Nano-Spectroscopy and -Imaging. *Surf. Sci. Rep.* **2020**, *75* (3), 100493.

(4) Fei, Z.; Rodin, A. S.; Andreev, G. O.; Bao, W.; McLeod, A. S.; Wagner, M.; Zhang, L. M.; Zhao, Z.; Thiemens, M.; Dominguez, G.; Fogler, M. M.; Neto, A. H. C.; Lau, C. N.; Keilmann, F.; Basov, D. N. Gate-Tuning of Graphene Plasmons Revealed by Infrared Nano-Imaging. *Nature* **2012**, *487* (7405), 82−85.

(5) Chen, J.; Badioli, M.; Alonso-González, P.; Thongrattanasiri, S.; Huth, F.; Osmond, J.; Spasenović, M.; Centeno, A.; Pesquera, A.; Godignon, P.; Zurutuza Elorza, A.; Camara, N.; de Abajo, F. J. G.; Hillenbrand, R.; Koppens, F. H. L. Optical Nano-Imaging of Gate-Tunable Graphene Plasmons. *Nature* **2012**, *487* (7405), 77−81.

(6) Basov, D. N.; Fogler, M. M.; Garcia de Abajo, F. J. Polaritons in van Der Waals Materials. *Science* **2016**, *354* (6309), aag1992.

(7) Basov, D. N.; Asenjo-Garcia, A.; Schuck, P. J.; Zhu, X.; Rubio, A. Polariton Panorama. *Nanophotonics* **2020**, *10* (1), 549−577.

(8) Fali, A.; White, S. T.; Folland, T. G.; He, M.; Aghamiri, N. A.; Liu, S.; Edgar, J. H.; Caldwell, J. D.; Haglund, R. F.; Abate, Y. Refractive Index-Based Control of Hyperbolic Phonon-Polariton Propagation. *Nano Lett.* **2019**, *19* (11), 7725−7734.

(9) de Oliveira, T. V. A. G.; Nörenberg, T.; Álvarez-Pérez, G.; Wehmeier, L.; Taboada-Gutiérrez, J.; Obst, M.; Hempel, F.; Lee, E. J. H.; Klopf, J. M.; Errea, I.; Nikitin, A. Y.; Kehr, S. C.; Alonso-González, P.; Eng, L. M. Nanoscale-Confined Terahertz Polaritons in a van Der Waals Crystal. *Adv. Mater.* **2021**, *33* (2), 2005777.

(10) Nörenberg, T.; Álvarez-Pérez, G.; Obst, M.; Wehmeier, L.; Hempel, F.; Klopf, J. M.; Nikitin, A. Y.; Kehr, S. C.; Eng, L. M.; Alonso-González, P.; de Oliveira, T. V. A. G. Germanium Monosulfide as a Natural Platform for Highly Anisotropic THz Polaritons. *ACS Nano* **2022**, *16* (12), 20174−20185.

(11) Sternbach, A. J.; Moore, S. L.; Rikhter, A.; Zhang, S.; Jing, R.; Shao, Y.; Kim, B. S. Y.; Xu, S.; Liu, S.; Edgar, J. H.; Rubio, A.; Dean, C.; Hone, J.; Fogler, M. M.; Basov, D. N. Negative Refraction in Hyperbolic Hetero-Bicrystals. *Science* **2023**, *379* (6632), 555−557.

(12) Hu, H.; Chen, N.; Teng, H.; Yu, R.; Xue, M.; Chen, K.; Xiao, Y.; Qu, Y.; Hu, D.; Chen, J.; Sun, Z.; Li, P.; de Abajo, F. J. G.; Dai, Q. Gate-Tunable Negative Refraction of Mid-Infrared Polaritons. *Science* **2023**, *379* (6632), 558−561.

(13) Zhang, Q.; Hu, G.; Ma, W.; Li, P.; Krasnok, A.; Hillenbrand, R.; Alù, A.; Qiu, C.-W. Interface Nano-Optics with van Der Waals Polaritons. *Nature* **2021**, *597* (7875), 187−195.

(14) Khatib, O.; Bechtel, H. A.; Martin, M. C.; Raschke, M. B.; Carr, G. L. Far Infrared Synchrotron Near-Field Nanoimaging and Nanospectroscopy. *ACS Photonics* **2018**, *5* (7), 2773−2779.

(15) Barcelos, I. D.; Bechtel, H. A.; de Matos, C. J. S.; Bahamon, D. A.; Kaestner, B.; Maia, F. C. B.; Freitas, R. O. Probing Polaritons in 2D Materials with Synchrotron Infrared Nanospectroscopy. *Adv. Opt. Mater.* **2020**, *8* (5), 1901091.

(16) Feres, F. H.; Mayer, R. A.; Wehmeier, L.; Maia, F. C. B.; Viana, E. R.; Malachias, A.; Bechtel, H. A.; Klopf, J. M.; Eng, L. M.; Kehr, S. C.; González, J. C.; Freitas, R. O.; Barcelos, I. D. Sub-Diffractional Cavity Modes of Terahertz Hyperbolic Phonon Polaritons in Tin Oxide. *Nat. Commun.* **2021**, *12* (1), 1995.

(17) Wehmeier, L.; Lang, D.; Liu, Y.; Zhang, X.; Winnerl, S.; Eng, L. M.; Kehr, S. C. Polarization-Dependent near-Field Phonon Nanoscopy of Oxides: $SrTiO_3$, $LiNbO_3$, and $PbZr_{0.2}Ti_{0.8}O_3$. *Phys. Rev. B* **2019**, *100* (3), 035444.

(18) Wehmeier, L.; Nörenberg, T.; de Oliveira, T. V. A. G.; Klopf, J. M.; Yang, S.-Y.; Martin, L. W.; Ramesh, R.; Eng, L. M.; Kehr, S. C. Phonon-Induced near-Field Resonances in Multiferroic $BiFeO_3$ Thin Films at Infrared and THz Wavelengths. *Appl. Phys. Lett.* **2020**, *116* (7), 071103.

(19) Yu, S.-J.; Jiang, Y.; Roberts, J. A.; Huber, M. A.; Yao, H.; Shi, X.; Bechtel, H. A.; Gilbert Corder, S. N.; Heinz, T. F.; Zheng, X.; Fan, J. A. Ultrahigh-Quality Infrared Polaritonic Resonators Based on Bottom-Up-Synthesized van Der Waals Nanoribbons. *ACS Nano* **2022**, *16* (2), 3027−3035.

(20) Yao, Z.; Chen, X.; Wehmeier, L.; Xu, S.; Shao, Y.; Zeng, Z.; Liu, F.; Mcleod, A. S.; Gilbert Corder, S. N.; Tsuneto, M.; Shi, W.; Wang, Z.; Zheng, W.; Bechtel, H. A.; Carr, G. L.; Martin, M. C.; Zettl, A.; Basov, D. N.; Chen, X.; Eng, L. M.; Kehr, S. C.; Liu, M. Probing Subwavelength In-Plane Anisotropy with Antenna-Assisted Infrared Nano-Spectroscopy. *Nat. Commun.* **2021**, *12* (1), 2649.

(21) Longuinhos, R.; Cadore, A. R.; Bechtel, H. A.; J S De Matos, C.; Freitas, R. O.; Ribeiro-Soares, J.; Barcelos, I. D. Raman and Far-Infrared Synchrotron Nanospectroscopy of Layered Crystalline Talc: Vibrational Properties, Interlayer Coupling, and Symmetry Crossover. *J. Phys. Chem. C* **2023**, *127* (12), 5876−5885.

(22) Liewald, C.; Mastel, S.; Hesler, J.; Huber, A. J.; Hillenbrand, R.; Keilmann, F. All-Electronic Terahertz Nanoscopy. *Optica* **2018**, *5* (2), 159−163.

(23) Chen, X.; Liu, X.; Guo, X.; Chen, S.; Hu, H.; Nikulina, E.; Ye, X.; Yao, Z.; Bechtel, H. A.; Martin, M. C.; Carr, G. L.; Dai, Q.; Zhuang, S.; Hu, Q.; Zhu, Y.; Hillenbrand, R.; Liu, M.; You, G. THz Near-Field Imaging of Extreme Subwavelength Metal Structures. *ACS Photonics* **2020**, *7* (3), 687−694.

(24) Schäffer, S.; Ogolla, C. O.; Loth, Y.; Haeger, T.; Kreusel, C.; Runkel, M.; Riedl, T.; Butz, B.; Wigger, A. K.; Bolívar, P. H. Imaging the Terahertz Nanoscale Conductivity of Polycrystalline $CsPbBr_3$ Perovskite Thin Films. *Nano Lett.* **2023**, *23* (6), 2074−2080.

(25) Aghamiri, N. A.; Huth, F.; Huber, A. J.; Fali, A.; Abate, Y.; Hillenbrand, R.; Abate, Y. Hyperspectral Time-Domain Terahertz Nano-Imaging. *Opt. Express* **2019**, *27* (17), 24231−24242.

(26) Moon, K.; Park, H.; Kim, J.; Do, Y.; Lee, S.; Lee, G.; Kang, H.; Han, H. Subsurface Nanoimaging by Broadband Terahertz Pulse Near-Field Microscopy. *Nano Lett.* **2015**, *15* (1), 549−552.

(27) Stinson, H. T.; Sternbach, A.; Najera, O.; Jing, R.; Mcleod, A. S.; Slusar, T. V.; Mueller, A.; Anderegg, L.; Kim, H. T.; Rozenberg, M.; Basov, D. N. Imaging the Nanoscale Phase Separation in Vanadium Dioxide Thin Films at Terahertz Frequencies. *Nat. Commun.* **2018**, *9* (1), 3604.

(28) Zhang, J.; Chen, X.; Mills, S.; Ciavatti, T.; Yao, Z.; Mescall, R.; Hu, H.; Semenenko, V.; Fei, Z.; Li, H.; Perebeinos, V.; Tao, H.; Dai, Q.; Du, X.; Liu, M. Terahertz Nanoimaging of Graphene. *ACS Photonics* **2018**, *5* (7), 2645−2651.

(29) Jing, R.; Shao, Y.; Fei, Z.; Lo, C. F. B.; Vitalone, R. A.; Ruta, F. L.; Staunton, J.; Zheng, W. J.-C.; Mcleod, A. S.; Sun, Z.; Jiang, B.; Chen, X.; Fogler, M. M.; Millis, A. J.; Liu, M.; Cobden, D. H.; Xu, X.; Basov, D. N. Terahertz Response of Monolayer and Few-Layer WTe_2 at the Nanoscale. *Nat. Commun.* **2021**, *12* (1), 5594.

(30) Borak, A. Toward Bridging the Terahertz Gap with Silicon-Based Lasers. *Science* **2005**, *308* (5722), 638−639.

(31) Huber, A. J.; Keilmann, F.; Wittborn, J.; Aizpurua, J.; Hillenbrand, R. Terahertz Near-Field Nanoscopy of Mobile Carriers in Single Semiconductor Nanodevices. *Nano Lett.* **2008**, *8* (11), 3766−3770.

(32) Pogna, E. A. A.; Viti, L.; Politano, A.; Brambilla, M.; Scamarcio, G.; Vitiello, M. S. Mapping Propagation of Collective Modes in Bi_2Se_3 and $Bi_2Te_{2.2}Se_{0.8}$ Topological Insulators by near-Field Terahertz Nanoscopy. *Nat. Commun.* **2021**, *12* (1), 6672.

(33) Chen, S.; Bylinkin, A.; Wang, Z.; Schnell, M.; Chandan, G.; Li, P.; Nikitin, A. Y.; Law, S.; Hillenbrand, R. Real-Space Nanoimaging of THz Polaritons in the Topological Insulator Bi_2Se_3. *Nat. Commun.* **2022**, *13* (1), 1374.

(34) Barnett, J.; Wehmeier, L.; Heßler, A.; Lewin, M.; Pries, J.; Wuttig, M.; Klopf, J. M.; Kehr, S. C.; Eng, L. M.; Taubner, T. Far-Infrared Near-Field Optical Imaging and Kelvin Probe Force Microscopy of Laser-Crystallized and -Amorphized Phase Change Material $Ge_3Sb_2Te_6$. *Nano Lett.* **2021**, *21* (21), 9012−9020.

(35) Kuschewski, F.; von Ribbeck, H.-G.; Döring, J.; Winnerl, S.; Eng, L. M.; Kehr, S. C. Narrow-Band near-Field Nanoscopy in the Spectral Range from 1.3 to 8.5 THz. *Appl. Phys. Lett.* **2016**, *108* (11), 113102.

(36) Feres, F. H.; Barcelos, I. D.; Cadore, A. R.; Wehmeier, L.; Nörenberg, T.; Mayer, R. A.; Freitas, R. O.; Eng, L. M.; Kehr, S. C.; Maia, F. C. B. Graphene Nano-Optics in the Terahertz Gap. *Nano Lett.* **2023**, *23* (9), 3913−3920.

(37) Giordano, M. C.; Mastel, S.; Liewald, C.; Columbo, L. L.; Brambilla, M.; Viti, L.; Politano, A.; Zhang, K.; Li, L.; Davies, A. G.; Linfield, E. H.; Hillenbrand, R.; Keilmann, F.; Scamarcio, G.; Vitiello, M. S. Phase-Resolved Terahertz Self-Detection near-Field Microscopy. *Opt. Express* **2018**, *26* (14), 18423.

(38) Degl'Innocenti, R.; Wallis, R.; Wei, B.; Xiao, L.; Kindness, S. J.; Mitrofanov, O.; Braeuninger-Weimer, P.; Hofmann, S.; Beere, H. E.; Ritchie, D. A. Terahertz Nanoscopy of Plasmonic Resonances with a Quantum Cascade Laser. *ACS Photonics* **2017**, *4* (9), 2150−2157.

(39) Knoll, B.; Keilmann, F. Enhanced Dielectric Contrast in Scattering-Type Scanning near-Field Optical Microscopy. *Opt. Commun.* **2000**, *182* (4−6), 321−328.

(40) Amarie, S.; Keilmann, F. Broadband-Infrared Assessment of Phonon Resonance in Scattering-Type near-Field Microscopy. *Phys. Rev. B* **2011**, *83* (4), 045404.

(41) Chu, J.; Xu, S.; Tang, D. Energy Gap versus Alloy Composition and Temperature in $Hg_{1-x}Cd_xTe$. *Appl. Phys. Lett.* **1983**, *43* (11), 1064−1066.

(42) Dumas, P.; Carr, G. L. *Infrared Spectroscopy and Spectro-Microscopy with Synchrotron Radiation*; Brookhaven National Lab: Upton, NY, United States, 2020.

(43) Schmit, J. L.; Stelzer, E. L. Temperature and Alloy Compositional Dependences of the Energy Gap of $Hg_{1-x}Cd_xTe$. *J. Appl. Phys.* **1969**, *40* (12), 4865−4869.

(44) Scott, M. W. Energy Gap in $Hg_{1-x}Cd_xTe$ by Optical Absorption. *J. Appl. Phys.* **1969**, *40* (10), 4077−4081.

(45) Faye, M.; Bordessoule, M.; Kanouté, B.; Brubach, J.-B.; Roy, P.; Manceron, L. Improved Mid Infrared Detector for High Spectral or Spatial Resolution and Synchrotron Radiation Use. *Rev. Sci. Instrum.* **2016**, *87* (6), 063119.

(46) Querry, M. R.. *Optical Constants of Minerals and Other Materials from the Millimeter to the Ultraviolet*;, Contractor Report CRDEC-CR-88009; 1987. https://apps.dtic.mil/sti/citations/ADA192210 (accessed 2023−06−25).

(47) Kaiser, W.; Spitzer, W. G.; Kaiser, R. H.; Howarth, L. E. Infrared Properties of CaF_2, SrF_2, and BaF_2. *Phys. Rev.* **1962**, *127* (6), 1950−1954.

(48) Hillenbrand, R.; Taubner, T.; Keilmann, F. Phonon-Enhanced Light-Matter Interaction at the Nanometre Scale. *Nature* **2002**, *418* (6894), 159−162.

(49) Taubner, T.; Hillenbrand, R.; Keilmann, F. Performance of Visible and Mid-Infrared Scattering-Type near-Field Optical Microscopes. *J. Microsc.* **2003**, *210* (3), 311−314.

(50) Keilmann, F.; Hillenbrand, R. Near-Field Microscopy by Elastic Light Scattering from a Tip. *Philos. Trans. R. Soc., A* **2004**, *362* (1817), 787−805.

(51) Deneuville, A.; Tanner, D.; Holloway, P. H. Optical Constants of ZnSe in the Far Infrared. *Phys. Rev. B* **1991**, *43* (8), 6544−6550.

(52) McArdle, P.; Lahneman, D. J.; Biswas, A.; Keilmann, F.; Qazilbash, M. M. Near-Field Infrared Nanospectroscopy of Surface Phonon-Polariton Resonances. *Phys. Rev. Res.* **2020**, *2* (2), 023272.

(53) Wang, H.; Wang, L.; Jakob, D. S.; Xu, X. G. Tomographic and Multimodal Scattering-Type Scanning near-Field Optical Microscopy with Peak Force Tapping Mode. *Nat. Commun.* **2018**, *9* (1), 2005.

(54) Ulaganathan, R. K.; Lu, Y.-Y.; Kuo, C.-J.; Tamalampudi, S. R.; Sankar, R.; Boopathi, K. M.; Anand, A.; Yadav, K.; Mathew, R. J.; Liu, C.-R.; Chou, F. C.; Chen, Y.-T. High Photosensitivity and Broad Spectral Response of Multi-Layered Germanium Sulfide Transistors. *Nanoscale* **2016**, *8* (4), 2284−2292.

(55) Zhang, S.; Wang, N.; Liu, S.; Huang, S.; Zhou, W.; Cai, B.; Xie, M.; Yang, Q.; Chen, X.; Zeng, H. Two-Dimensional GeS with Tunable Electronic Properties via External Electric Field and Strain. *Nanotechnology* **2016**, *27* (27), 274001.

(56) Ding, G.; Gao, G.; Yao, K. High-Efficient Thermoelectric Materials: The Case of Orthorhombic IV-VI Compounds. *Sci. Rep.* **2015**, *5* (1), 9567.

(57) Fei, R.; Kang, W.; Yang, L. Ferroelectricity and Phase Transitions in Monolayer Group-IV Monochalcogenides. *Phys. Rev. Lett.* **2016**, *117* (9), 097601.

(58) Sutter, P.; Wimer, S.; Sutter, E. Chiral Twisted van Der Waals Nanowires. *Nature* **2019**, *570* (7761), 354−357.

(59) Wiley, J. D.; Buckel, W. J.; Schmidt, R. L. Infrared Reflectivity and Raman Scattering in GeS. *Phys. Rev. B* **1976**, *13* (6), 2489−2496.

(60) Yu, L.-M.; Degiovanni, A.; Thiry, P. A.; Ghijsen, J.; Caudano, R.; Lambin, Ph. Infrared Optical Constants of Orthorhombic IV-VI Lamellar Semiconductors Refined by a Combined Study Using Optical and Electronic Spectroscopies. *Phys. Rev. B* **1993**, *47* (24), 16222−16228.

(61) Mihajlovic, P.; Nikolic, P. M.; Hughes, O. H. Infrared Reflectivity of GeS. *J. Phys. C: Solid State Phys.* **1976**, *9* (21), L599−L602.

(62) Alonso-González, P.; Nikitin, A. Y.; Gao, Y.; Woessner, A.; Lundeberg, M. B.; Principi, A.; Forcellini, N.; Yan, W.; Vélez, S.; Huber, A. J.; Watanabe, K.; Taniguchi, T.; Casanova, F.; Hueso, L. E.; Polini, M.; Hone, J.; Koppens, F. H. L.; Hillenbrand, R. Acoustic Terahertz Graphene Plasmons Revealed by Photocurrent Nanoscopy. *Nat. Nanotechnol.* **2017**, *12* (1), 31−35.

(63) Döring, J.; Lang, D.; Wehmeier, L.; Kuschewski, F.; Nörenberg, T.; Kehr, S. C.; Eng, L. M. Low-Temperature Nanospectroscopy of the Structural Ferroelectric Phases in Single-Crystalline Barium Titanate. *Nanoscale* **2018**, *10* (37), 18074−18079.

(64) Yang, H. U.; Hebestreit, E.; Josberger, E. E.; Raschke, M. B. A Cryogenic Scattering-Type Scanning near-Field Optical Microscope. *Rev. Sci. Instrum.* **2013**, *84* (2), 023701.

(65) McLeod, A. S.; van Heumen, E.; Ramirez, J. G.; Wang, S.; Saerbeck, T.; Guenon, S.; Goldflam, M.; Anderegg, L.; Kelly, P.; Mueller, A.; Liu, M. K.; Schuller, I. K.; Basov, D. N. Nanotextured Phase Coexistence in the Correlated Insulator V_2O_3. *Nat. Phys.* **2017**, *13* (1), 80−86.

(66) Luo, W.; Boselli, M.; Poumirol, J.-M.; Ardizzone, I.; Teyssier, J.; van der Marel, D.; Gariglio, S.; Triscone, J.-M.; Kuzmenko, A. B. High Sensitivity Variable-Temperature Infrared Nanoscopy of Conducting Oxide Interfaces. *Nat. Commun.* **2019**, *10* (1), 2774.

(67) Dong, Y.; Xiong, L.; Phinney, I. Y.; Sun, Z.; Jing, R.; McLeod, A. S.; Zhang, S.; Liu, S.; Ruta, F. L.; Gao, H.; Dong, Z.; Pan, R.; Edgar, J. H.; Jarillo-Herrero, P.; Levitov, L. S.; Millis, A. J.; Fogler, M. M.; Bandurin, D. A.; Basov, D. N. Fizeau Drag in Graphene Plasmonics. *Nature* **2021**, *594* (7864), 513−516.

(68) Zhao, W.; Zhao, S.; Li, H.; Wang, S.; Wang, S.; Utama, M. I. B.; Kahn, S.; Jiang, Y.; Xiao, X.; Yoo, S.; Watanabe, K.; Taniguchi, T.; Zettl, A.; Wang, F. Efficient Fizeau Drag from Dirac Electrons in Monolayer Graphene. *Nature* **2021**, *594* (7864), 517−521.

(69) Dapolito, M.; Tsuneto, M.; Zheng, W.; Wehmeier, L.; Xu, S.; Chen, X.; Sun, J.; Du, Z.; Shao, Y.; Jing, R.; Zhang, S.; Bercher, A.; Dong, Y.; Halbertal, D.; Ravindran, V.; Zhou, Z.; Petrovic, M.; Gozar, A.; Carr, G. L.; Li, Q.; Kuzmenko, A. B.; Fogler, M. M.; Basov, D. N.; Du, X.; Liu, M. Infrared Nano-Imaging of Dirac Magnetoexcitons in Graphene. *Nat. Nanotechnol.* **2023**, 1−7.

(70) Kim, R. H. J.; Park, J.-M.; Haeuser, S. J.; Luo, L.; Wang, J. A Sub-2 Kelvin Cryogenic Magneto-Terahertz Scattering-Type Scanning near-Field Optical Microscope (Cm-THz-sSNOM). *Review of Scientific Instruments* **2023**, *94* (4), 043702.

(71) Sun, Z.; Fogler, M. M.; Basov, D. N.; Millis, A. J. Collective Modes and Terahertz Near-Field Response of Superconductors. *Phys. Rev. Res.* **2020**, *2* (2), 023413.

(72) Park, S.; Yager, K. Roll-to-Roll Mechanized Exfoliator and Automatic 2D Materials Transfer and Layering System. Patent application number PCT/US2022/040777, WO 2023023260 A2, August 18, 2022. https://patentimages.storage.googleapis.com/f2/f1/5c/46f830a8af203b/WO2023023260A2.pdf (accessed 2023−06−26).